Fully automated segmentation of carotid and vertebral arteries from CTA

Release 0.00

Olivier Cuisenaire

July 20, 2009

olivier.cuisenaire@philips.com
Medisys Research Lab
Philips Healthcare
92150 Suresnes, France

Abstract

We propose a method for segmenting and labeling the main head and neck vessels (common, internal, external carotid, vertebral) from a contrast enhanced computed tomography angiography (CTA) volume. First, an initial centerline of each vessel is extracted. Next, the vessels are segmented using 3D active objects initialized using the first step. Finally, the true centerline is identified by smoothly deforming it away from the segmented mask edges using a spline-snake.

We focus particularly on the initial centerline extraction technique. It uses a locally adaptive front propagation algorithm that attempts to find the optimal path connecting the ends of the vessel, typically from the lowest image of the scan to the Circle of Willis in the brain. It uses a patient adapted anatomical model of the different vessels both to initialize and constrain this fast marching, thus eliminating the need for manual selection of seed points.

The method is evaluated by applying it to the MICCAI 2009 carotid bifurcation challenge datasets.

Latest version available at the Insight Journal [http://hdl.handle.net/10380/1338]

Contents

Extracting vessels from image volumes is a key requirement for the display and analysis of CT angiography studies. Indeed, vessel centerlines are needed to create curved multi-planar reformatted (cMPR) views - where the whole vessel is visible in a single 2D image - or to display vessel cross-sections. Segmented vessel masks are useful for quantitative analysis of pathologies, such as stenoses, plaque or aneurysms. These vessel masks can also be used to remove the bony structures from 3D rendered images, without resorting to image subtraction between a contrast-enhanced and a noncontrast image dataset, thus reducing patient radiation dose and avoiding registration error artifacts. Bone masking is particularly challenging for the vessels in the neck region, since the internal carotid goes through the base of the skull, the vertebral arteries cross through the cervical vertebrae, and the basilar artery closely follows the occipital bone.

Vessel extraction can be performed in many different ways, as discussed by Kirbas et al [4]. A widely used approach consists of splitting the problem into two steps. First step involves an approximation of the vessel centerline. It is for instance, defined as the path of minimal cost between user-selected seed points [3, 6, 8]. Then, this centerline is used to initialize the segmentation of the whole vessel [1]. In other cases, these two steps are iterated, partial segmentation results in helping to estimate the local vessel direction and drive the centerline definition [7, 5]. This segmentation step is most often performed using geodesic active surfaces.

A major limitation of these methods is that, in order to extract a specific vessel, they typically require user interaction in the form of one [5] or more seed points placed in the vessel to be extracted. This precludes preprocessing the data before human inspection and therefore slows down the clinical workflow. These methods also typically require significant computational time in the order of several minutes per segmented vessel. This is a serious limitation for the use of these methods in clinical practice.

The purpose of this paper is to present and validate a vessel extraction method that overcomes both limitations (i.e., is the method should be fully automatic with low computational cost). To this purpose, we adapt the minimal paths method of Deschamps and Cohen [3] to the specific needs of neck CTA. Manual seeding of the centerline extraction method is replaced by patient adapted vessel seeding models. Finally, segmentation is performed using explicit active surfaces.

This method was previously presented in [2], with a focus on its ability to improve the workflow. It automatically provides vessel centerlines for MPR visualization, as well as masks for bone-suppressed MIP and volume rendering. Processing times of only a couple of minutes to extract all the vessels at once (common, internal and external carotids, vertebral and basiliar arteries) and the possibility to preprocess the data given the absence of user input allow us to present the physician with improved visualization possibilites without any delay in the workflow. In this paper, we test the ability of this method to also provide automatic quantitative measurements on the datasets of the MICCAI 2009 carotid bifurcation segmentation challenge.

1 Method

Vessel extraction and labeling is performed in several steps. First, we construct a model for each of the vessels we want to extract. This model consists of multiple estimates for the beginning and end points of the

vessel and a set of walls that the vessel cannot cross. Then, an initial centerline of each vessel is extracted by searching a minimal path between these beginning and end points. Finally, the vessels are segmented using 3D active objects initialized using the initial centerline. Note that later on, the true centerline can be obtained by smoothly deforming the original centerline away from the segmented mask edges using a spline-snake, but this is not discussed in this paper.

1.1 Supervised vessel extraction

For the sake of clarity, let us start with the second step (i.e. the extraction of an initial vessel centerline assuming that we know its beginning and end points). This is what would happen with user-specified seeds x_b and x_e. In this case, as in [2], the best path connecting those points is defined as the path $C(s)$ that minimizes the energy

$$E(C) = \int_0^L (w + P(C(s)))ds = \int_0^L \tilde{P}(C(s))ds \tag{1}$$

where $C(s)$ represents a 1D curve of unknown length L in the 3D CT volume, $P(x)$ is appropriately chosen to have low values when x is a vessel voxel and higher values otherwise, and w is a constant regularization factor that favors shorter paths. Both $P(x)$ and w have positive values. Since C is a path linking the specified end points x_b and x_e, we have $C(0) = x_b$ and $C(L) = x_e$

While minimizing $E(C(s))$ over all possible paths C may appear computationally expensive, it can be done quite efficiently by fast marching (i.e. by computing the action map from x_b)

$$U_b(C) = \min_{C(0)=x_b, C(L')=x} E(C) = \min \int_0^{L'} \tilde{P}(C(s))ds \tag{2}$$

One can show that this action map respects the Eikonal equation

$$\|\nabla U_b\| = \tilde{P} \tag{3}$$

as well as the initial condition $U_b(x_b) = 0$. Equation 2 can therefore be computed by an upwind finite difference scheme, starting from $U_b(x_b) = 0$ for the first seed, until the propagation front reaches the target x_e. The best path is then extracted from U by backtracking the propagation down to the first seed, i.e. starting with $C(L) = x_e$, then choosing $C(L-1)$ as the neighboring voxel of x_e with the lowest value of U, and iterating until we reach the minimum value of U as $U_b(x_b) = 0$.

A more efficient alternative consists of propagating two different action maps U_b and U_e from both seed points. When the two propagation fronts collide in a point x_c, the best path is found as the union of the two paths from x_c to x_b, and x_c to x_e.

Choosing $\tilde{P}(x)$ appropriately is of the utmost importance. It is particularly tricky as the appearance of the vessels varies greatly over their course through the neck and head. In the neck, carotids appear as bright cylindrical objects on a dark background. As they cross the skull base, they become curvy and appear darker than the surrounding bones. Vertebral arteries alternate between dark and bright background as

they go through the different vertebrae, and appear as both straight and curvy portions. The basilar artery typically has bright bone on one side and dark brain tissue on the other side. In addition, the concentration of the contrast agent which gives the vessel its higher HU values varies throughout the course of the vessel depending on the timing of the scan with regard to the injection of the bolus. Due to these many sources of variation, any single measure of vesselness is bound to fail at some point of the vessel path. Instead, we use a combination of factors in the form of

$$\tilde{P}(x) = \sum w_i P_i(x)^{\alpha_i} \tag{4}$$

including classical vesselness functions based on the Hessian, but also simpler ones that favor a reasonable range of HU values, penalize gradient, and favor local maxima. We also build a model of the expected local HU value of the contrast agent inside the vessel by locally backtracking U to create local estimates of the vessels centerline. This actually makes $\tilde{P}(x)$ dependent not only on the location x but also on how it was reached by U, which may appear considerably more complex mathematically, but can be implemented in a very straightforward manner. Parameters w_i and α_i are determined experimentally.

1.2 Vessel models for unsupervised centerline extraction

Let us now assume that we do not have user-selected end points for the vessel we want to extract. In order to be able to use the above method, we need an automated method to choose such points. Unfortunately, it is unrealistic to expect to be able to find a single seed point at each end of the targeted vessel, because of the high anatomical, pathological or acquisition protocol variability encountered in practical cases. On the other hand, it is realistic to assume that we can define two small sets of candidate points $X_b = \{x_{b0}, x_{b1}, ...\}$ and $X_e = \{x_{e0}, x_{e1}, ...\}$ for two limited regions of interest around the expected ends of the vessel. In this case, we can reformulate the minimal path problem as the path $C(s)$ that minimizes the cost function in 1 under the constrains that $C(0) \in X_b$ and $C(L) \in X_e$. This new problem is as easily solved as before by rewriting 2 as

$$U_B(x) = \min_{C(0)\in X_b, C(L')=x} E(C) = \min \int_0^{L'} \tilde{P}(C(s))ds \tag{5}$$

by initializing $U_B(x) = 0, \forall x \in X_b$ and similarly for U_E. Once again, we can solve this by using an upwind finite difference scheme until both propagation fronts collide. Backtracking the propagation from this collision point defines which pair of seed points from X_b and X_e actually belongs to the vessel. The actual definition of the sets X_b and X_e is of course vessel dependent. The RICA (resp. LICA) model includes the right (resp. left) common and internal carotid arteries. X_b is located as low as possible in the neck, on the right (resp. left) side of the image with respect to the spine. X_e should be in the brain close to the circle of Willis. The exact location of X_e is found by registering a brain model onto the patient image and applying the resulting transform to the X_e of the model. The RVA (resp. LVA) model includes the right (resp. left) vertebral and basilar arteries. X_b is once again located as low as possible in the neck, on the right (resp. left) side of the image with respect to the spine, and within a reasonable distance of the spine. X_e is inside the brain, close to the circle of Willis, at an exact location found by registering using the brain model transform. Finally, the RECA (resp. LECA) model includes the right (resp. left) external carotid and maxillary arteries. X_b is made of the centerline of the common and internal carotid extracted using the first model, X_e is close to the face of the patient. Unfortunately, such definitions of X_b and X_e are not sufficient to ensure that the correct vessel is always found. Often, the carotid arteries will be found while trying to extract the vertebral arteries because, carotids being larger vessels, they tend to be easier paths to use. Similarly, when the image

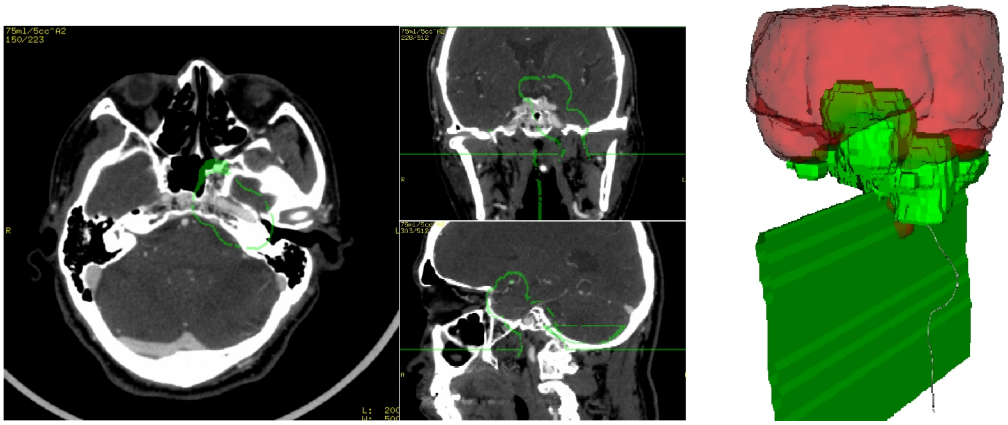

Figure 1: LICA vessel model for left common and internal carotid in green, segmented brain in red

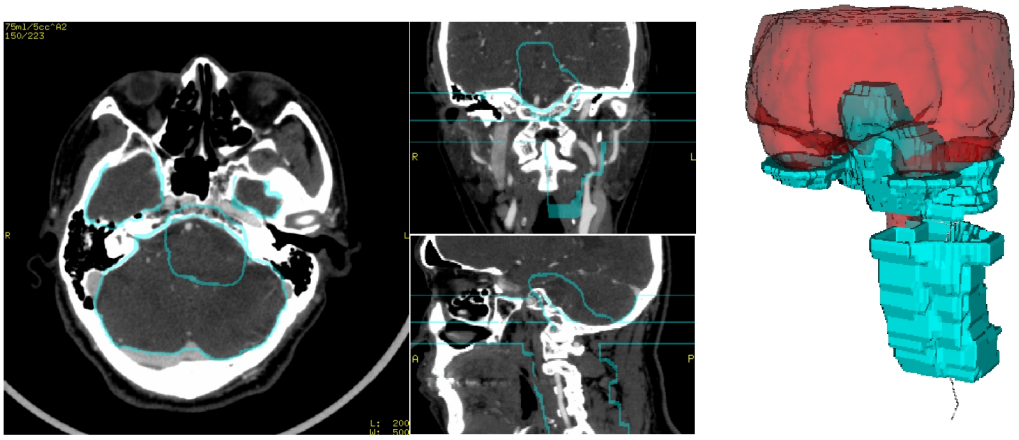

Figure 2: LVA vessel model for the left vertebral and basilar arteries in blue, segmented brain in red

is aquired too late after injection, the jugular veins can appear nearly as bright as the arteries and confuse the extraction algorithm. To prevent this, we add walls to the vessel models. These walls are sets of points where $\tilde{P}(x) = \infty$. This stops the propagation front when computing U and prevents the extracted vessels from crossing the walls. For each vessel model, specific walls were designed, primarily by learning from manually segmented vessels in 30 datasets from a variety of origins. These walls are illustrated in Figures 1 to 3 for the left vessels.

1.3 Segmentation using Active Surfaces

The extracted centerline is used to initialize the segmentation of the whole vessel mask. This is done using a 3D active surface that is explicitly implemented as a simplex mesh. Deformation of the mesh is driven by forces that attract the surface to the vessel edges using the local image curvature. It also uses a local estimate of the HU value of the contrast agent in the vessel. To achieve this, the mesh is divided in regions for which a different local force is defined depending on the observed HU values in the closest centerline voxels. The resulting deformation is illustrated at Figure 4.

The resulting segmentation is a little too smooth compared to the anatomical truth. Therefore, we perform two post processing steps on the resulting segmentation mask. First, a calcification removal step that de-

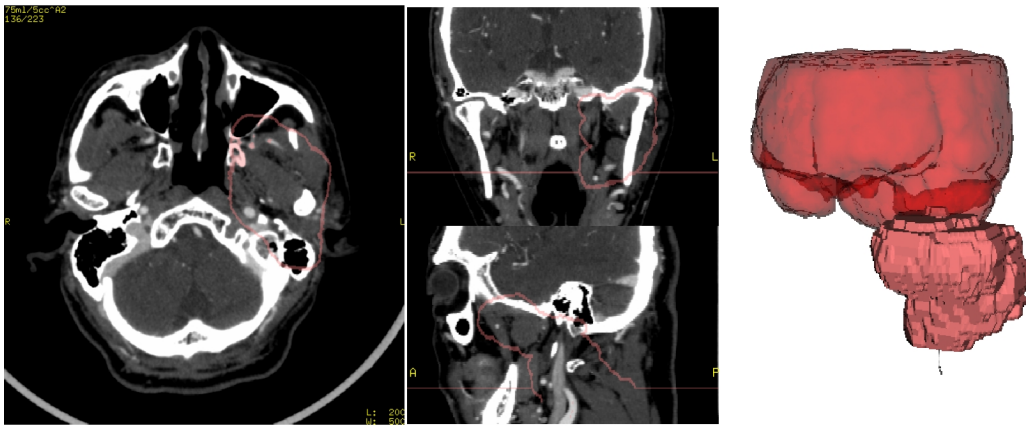

Figure 3: LECA vessel model for the left external carotid and maxillary arteries in pink, segmented brain in red

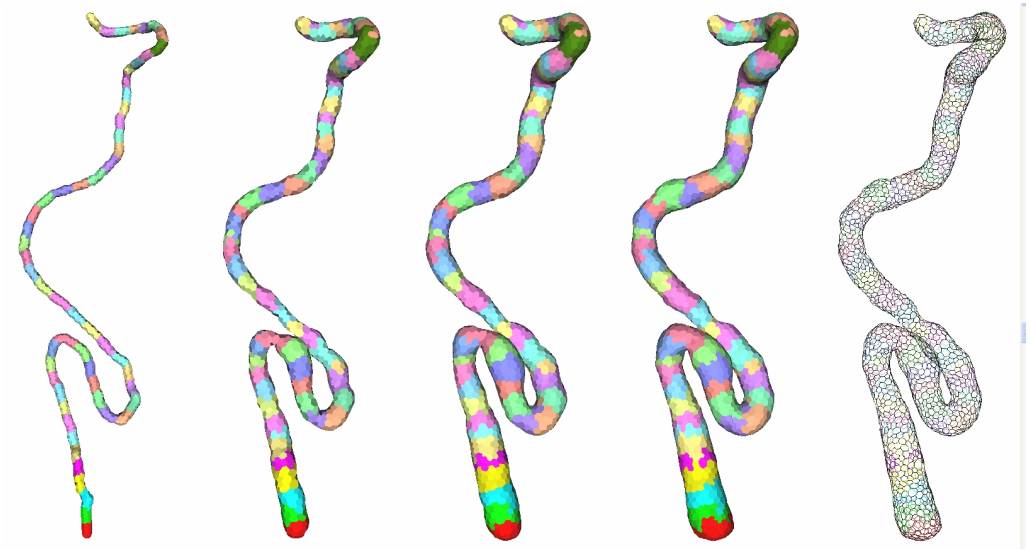

Figure 4: Evolution of the active contour segmentation algorithm, from a small tube around the approximate centerline on the left, to a fully segmented right internal carotid on the right. The rightmost mesh is visualized as a wireframe to better demonstrate the nature of the mesh. Colors correspond to different regions for the local estimation of the vessel HU value

Table 1: Training: Summary lumen

Measure	% / mm			rank		
	min.	max.	avg.	min.	max.	avg.
L_dice	88.0%	93.5%	91.3%	3	4	3.93
L_msd	0.07mm	0.20mm	0.12mm	1	4	2.73
L_rmssd	0.11mm	0.30mm	0.18mm	1	4	3.07
L_max	0.64mm	1.98mm	1.09mm	3	4	3.87
Total (lumen)				**1**	**4**	**3.40**

Table 2: Training: Averages lumen

Team	Total	dice		msd		rmssd		max		Total
name	success	%	rank	mm	rank	mm	rank	mm	rank	rank
Medisys	10	91.3	3.9	0.12	2.7	0.18	3.1	1.09	3.9	3.4
ObserverA	15	94.6	1.3	0.11	1.8	0.15	1.7	0.53	1.6	1.6
ObserverB	15	93.4	2.4	0.14	3.2	0.19	3.2	0.74	2.5	2.8
ObserverC	15	93.3	2.3	0.14	3.3	0.21	3.1	1.04	3.0	2.9

tects voxels that are significantly above the HU values found at the center of the vessel followed by region growing. Secondly, an analysis of a thin layer of voxels at the edge of the mask that assigns partial volume percentages voxel per voxel by comparing each voxel HU intensity to the typical HU found in the center of the vessel.

2 Results

In [2], the method was validated by applying it to a database of 28 scans from multiple regions (USA, India, China, Israel) including a variety of scanners (10, 16, 40, 64-slice; Brilliance CT, Philips Healthcare, Cleveland, OH, USA), contrast agent dose, and image resolution. This included scans with severe metal artifacts and a variety of anatomical variations and pathologies. Three medical experts were shown curved MPRs computed using the extracted centerlines as well as maximum intensity projection (MIP) and volume rendered images computed using the segmented masks. They rated each case on a variety of criteria such as the success or failure to find the appropriate vessel, or the presence or absence of bone remnants in the segmentation masks. The 6 modeled vessels were all successfully extracted in 93% of the patients. In the other cases, manual seeding provided an efficient alternative for the vessels that were missed or inaccurately extracted. Vessel extraction is robust to dental and other metal artifacts in the neck region. It is robust to anatomical variability, such as height of the carotid bifurcation or the presence of loops in the neck vessels. It is robust to pathological variability, such as the presence of partial stenosis, calcification, or aneurysms, which are correctly segmented as part of the vessel. However, in the presence of total occlusion, manual seeding is usually required to recover the visible parts of the vessels.

For this paper, we applied our algorithms to the 15 training cases and 31 testing cases of the MICCAI challenge. The results are found in tables 1 to 4. We marked as failed all cases where the algorithm failed to properly extract and segment any part of the vessels in the region of interest around the carotid bifurcation, even if it did succeed for the most part. With this strict definition of success and failure, we could successfully process 10 out of 15 cases in the training datasets and 23 out of 31 testing cases.

For those successful cases, the average mean surfaces distances and root mean squared surface distances were $0.12mm$ and $0.18mm$ respectively for the training datasets (table 1), and $0.16mm$ and $0.21mm$ respectively for the testing datasets (table 3). This is similar to the performance of observers B and C for the training data (table 2) and only slightly worse for the testing data (table 4). It is also noticeably smaller than the voxel sizes in the different datasets, which varied between $0.12mm \times 0.12mm \times 0.30mm$ and $0.5mm \times 0.5mm \times 0.5mm$.

Table 3: Testing: Summary lumen

Measure	% / mm			rank		
	min.	max.	avg.	min.	max.	avg.
L_dice	87.4%	92.4%	90.3%	4	4	4.00
L_msd	0.09mm	0.29mm	0.16mm	2	4	3.84
L_rmssd	0.11mm	0.33mm	0.21mm	2	4	3.77
L_max	0.42mm	2.02mm	1.10mm	3	4	3.87
Total (lumen)				**2**	**4**	**3.87**

Table 4: Testing: Averages lumen

Team name	Total success	dice		msd		rmssd		max		Total rank
		%	rank	mm	rank	mm	rank	mm	rank	
Medisys	23	90.3	4.0	0.16	3.8	0.21	3.8	1.10	3.9	3.9
ObserverA	31	95.4	1.5	0.10	1.8	0.13	1.9	0.56	2.2	1.8
ObserverB	31	94.8	2.4	0.11	2.7	0.15	2.6	0.59	2.0	2.4
ObserverC	31	94.7	2.2	0.11	2.5	0.15	2.5	0.71	2.7	2.5

It is of course interesting to look more closely at the 8 testing cases where failure occured. First, let us note that cases 009 to 029 present a particular challenge to the method as the model fitting relies on the registration of the brain, which is only very partially present in the field of view chosen for reconstruction for these datasets, as illustrated at figure 5. Nevertheless, we are able to find a sufficient match in all cases to allow the method to proceed.

In cases 012 and 014, we extract the common and internal carotids properly, but fail to find the external carotids as the set of seed points X_e proposed by our model is placed outside the reconstruction field of view. We should be able to handle those cases properly in the on-site challenge using specific LECA and RECA models for datasets reconstructed using such a reduced field of view. In case 022, we extract the common and external carotids properly, but miss part of the RICA, as illustrated at figure 6. This is due to a combination of near total occlusion of the RICA and a late acquisition time that fills the jugular vein with contrast agent. This makes the vessel extraction algorithm take a shortcut through the vein to bypass the occlusion. While the algorithm should be able to overcome either of these problems, it fails against their combination. In case 024, we extract the internal carotid properly but fail to cross the heavily calcified bifurcation towards the common carotid.

In case 103, we extract the internal and external carotids properly, but fail to extract the common carotid due to the abnormaly high level of artefacts caused by shoulder bones without proper dose adaptation. In case 106, we fail to extract the internal carotid as it is nearly fully occluded after the bifuraction. Instead, the algorithm takes a shortcut through the external carotid that runs alongside the occlusion.

In case 205, the common carotid is 100% occluded and no blood reaches the brain through it, which obvi-

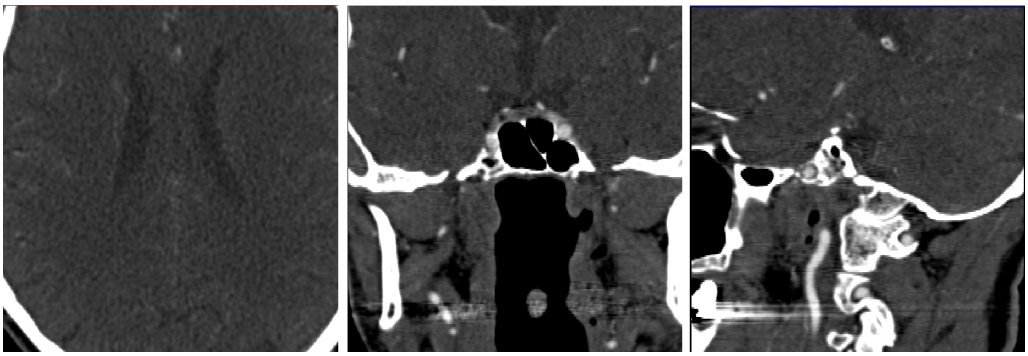

Figure 5: Reduced field of view around the brain for case 011, typical of the 0xx cases

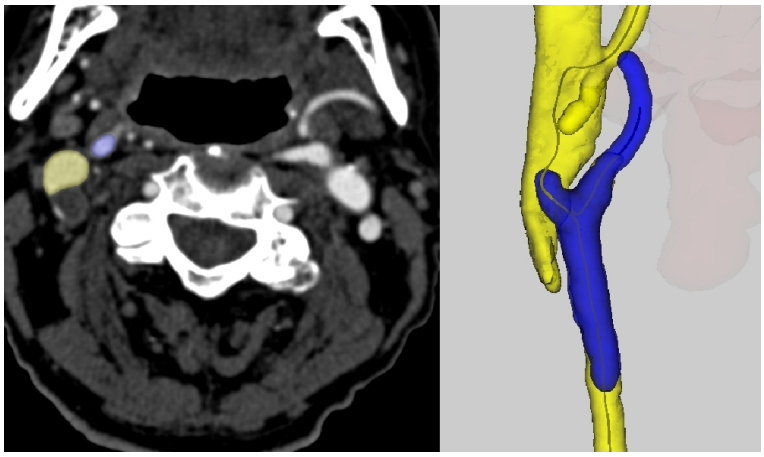

Figure 6: Case 022

ously makes our approach impractical and would require manual seeding instead. Besides, the acquisition timing illuminates the jugular veins as brightly as the arteries, so the algorithm extracts it instead. Finally, in case 206 all vessels centerlines are extracted properly, but the segmentation method is not appropriate for the very high level of noise and artifacts found at the bifurcation level and below due to the lack of dose adaptation to the presence of the shoulders.

3 Conclusion

We have developed and validated a fully automated vessel extraction and segmentation tool for CTA of the head and neck region. While the scope of the method is much wider as it can extract the carotids from the aortic arch to the circle of Willis as well as the vertebral arteries, this paper focuses on the small region of interest around the carotid bifurcation that is used for the MICCAI 2009 segmentation challenge. In this restricted context, the algorithm nevertheless achieves sub-voxel accuracy and performs close to the performance of manual observers. We believe its performance in terms of robustness and low computational complexity makes it directly applicable for clinical use.

References

[1] C. Van Bemmel, L. Spreeuwers, M. Viergever, and W. Niessen. Level-set based artery-vein separation in blood pool agent ce-mr angiograms. *IEEE Trans. Med. Im.*, 22(10):1224–1234, 2003. (document)

[2] O. Cuisenaire, S. Virmani, M.E. Olszewski, and R. Ardon. Fully automated segmentation of carotid and vertebral arteries from contrast enhanced cta. In J. M. Reinhardt and J. P. W. Pluim, editors, *SPIE Medical Imaging*, volume 6914. SPIE, 2008. (document), 2

[3] T. Deschamps and L. Cohen. Fast extraction of minimal paths in 3-d images and applications to virtual endoscopy. *Med. Im. Anal.*, 5(4):281–299, 2001. (document)

[4] C. Kirbas and F. Quek. A review of vessel extraction techniques and algorithms. *ACM Comp. Surv.*, 36(2):81–121, 2004. (document)

[5] R. Manniesing and M. Viergever. Vessel axis tracking using topology constrained surface evolution. *IEEE Trans. Med. Im.*, 26(3):309–316, 2007. (document)

[6] O. Wink, A. Frangi, B. Verdonk, M. Viegever, and W. Niessen. 3-d mra coronary axis determination using a minimum cost path approach. *Magn. Reson. Med.*, 47(6):1169–1174, 2002. (document)

[7] O. Wink, W. Niessen, and M. Viegever. Fast delineation and visualization of vessels in 3-d angiographic images. *IEEE Trans. Med. Im.*, 19(4):337–346, 2000. (document)

[8] O. Wink, W. Niessen, and M. Viergever. Multiscale vessel tracking. *IEEE Trans. Med. Im.*, 26(1):130–133, 2004. (document)